Supplementary Material: Computational Analysis of Enhanced Circulating Tumor Cell (CTC) Separation in a Microfluidic System with an Integrated Dielectrophoretic-Magnetophorectic (DEP-MAP) Technique

Wan-Shi Low and Nahrizul Adib Kadri

1. Design Requirements

In proposing a design of a CTC detection microfluidic device, the first step is to define the required specifications. To adequately mimic the operation of a real microfluidic system, our computational development strategy takes into careful consideration several experimental parameters, including sample size, developed channel flow pattern, optimum fluid mean velocity, uniformity of flow, material used, the generated electric and magnetic field gradient, and fabrication complexity. These parameters are described in the following:

1.1. Sample Volume and Cell Throughput

Sample volume plays an important role when designing a microfluidic channel. The relationship between sample volume (V) and analysed concentration is shown below [1]:

$$V = \frac{1}{\eta_S N_A A_i} \tag{S1}$$

where η_S indicates the sensor efficiency, N_A is Avogadro's number, and A_i is the analyte concentration. In spite of the small reagent volume required for analysis purposes, the microfluidic channel enables repetitive sampling at multiple time points, which in turn allows the isolation process to be conducted in a continuous-flow mode. However, the effect of a microfluidic volume challenges the efficiency of CTC detection whereby its presence ranges from 0–10 cells per millilitre of blood. Furthermore, the throughput achievable by microfluidic devices in average processes is around 1–3 mL of blood per hour [2,3]. Such an output is considered insufficient as it will take hours to complete the analysis, in the case that a 7.5 mL of whole blood sample from patients is generally employed for enumeration of CTC in diagnostic application. Consequently, there is a need for researchers to develop a microfluidic architecture which allows for high throughput, as well as enhancing the separation efficiency of CTCs. It is generally accepted that an instrument which makes analysis of CTCs for a clinically-relevant procedure should achieve processing of one sample in two hours [4]. In order to capture the optimal volume of the microfluidic channel without influencing the flow velocity and the microelectrode efficiency, the length of the DEP and MAP chamber is suggested to be in the range of 15–20 mm, with a channel height of 0.5–1 mm [1].

1.2. Optimum Fluid Mean Velocity

When a specimen is forced into the microfluidic channel, the hydrodynamic force (F_{HD}) applied on a cell is influenced by the flow velocity. It can be described with Stokes Law, as follows [5]:

$$\vec{F}_{HD} = 4\pi\eta\, R\vec{v} \tag{S2}$$

In which $\vec{v}$ is the relative velocity between the cell with a radius, R and the flow. This equation shows that the flow velocity is directly proportional to the hydrodynamic force.

It must be noted that apart from the hydrodynamic force, the cell will experience a MAP (F_{MAP}) or DEP (F_{DEP}) force in our proposed CTC capture micro-device. Therefore, as the cells are directed into the MAP or DEP microchamber, there are some points corresponding to the electrical or magnetic field gradient in the tangential direction relative to the flow. These forces cause deviation of the flow direction of the cells and direct them to their targeted outlet under F_{HD}. However, if the

applied flow rate is not strong enough to carry them through the channel, a **F**MAP or **F**DEP along the microfluidic length direction will keep them from the **F**HD of the flow and capture the cells in a series of virtual traps along the channel. Subsequently, it will result in an accumulation and suspension of cells along the channel. Such a condition is undesirable as it causes uneven electrical or magnetic field intensity to be measured during the cell separation analysis. In order for the flow to generate sufficient **F**HD to carry cells toward their designated outlet, the flow velocity must overcome the **F**MAP or **F**DEP along the length of the channel (*x*-direction). These flow parameters can be stated quantitatively by the following approximation:

$$v_{\min} < v_{\text{opt}} < v_{\max} \tag{S3}$$

whereby v_{opt} is referred to as the range of optimum flow velocity, $v_{\min}$ is the minimum flow velocity, and $v_{\max}$ is the maximum flow velocity. By relating both the formulation of DEP and MAP (refers to main text) with Equation (S2), the ideal flow rate in the cell capture application for the DEP and MAP stage can be alluded to respectively as:

DEP stage:

$$\frac{\varepsilon_m \varepsilon_0 R^2}{2\eta} \, Re[K(\omega)] \nabla \frac{\partial E^2}{\partial x} < v_{D\_opt} < \frac{lR^2}{2w\eta} \varepsilon_m \varepsilon_0 \, Re[K(\omega)] \nabla \frac{\partial E^2}{\partial y} \tag{S4}$$

MAP stage:

$$\frac{\mu_f \, (\chi_p - \chi_m) \, V_c \frac{\partial H_{ext}^2}{\partial x}}{4\pi\eta \, R} < v_{M\_opt} < \frac{l \, \mu_f \, (\chi_p - \chi_m) \, V_c \frac{\partial H_{ext}^2}{\partial y}}{4\pi\eta \, wR} \tag{S5}$$

where v_{D_opt} and v_{M_opt} are the optimum flow rates in the DEP and MAP stage, respectively. From the equation above, both the length and width of a DEP or MAP microchamber are shown to be correlated with the maximum flow velocity of the cell. As such, the smaller the width, the higher the flow rate that flow sthrough a channel to ensure cell separation with high throughput. Due to the constraint of an available micro-fabrication technique, the minimum allowed width of the channel will be fixed at 250 μm.

1.3. Electric Field Strength and Cell Residency Time in the DEP Stage

Because the electrical field will be scaled down favourably at the microscale, a high electric field can be generated using only a few volts within a DEP microchamber. A **F**DEP will increase with the square of the applied electric field gradient, thus making larger input voltages desirable for cell separation. It is noteworthy that the application of an external electric field on the living cell will cause a transmembrane voltage due to the accumulation of ions on the cell membrane surface [6]. The transmembrane voltage has been proved in the literature to be proportional to the cell radius. For instance, cells of larger radii such as breast CTCs can be electroporated at a smaller local field strength [7]. However, if the required DEP voltage is too high for large cancer cells to be attracted toward an electrode edge with a high field region, the transmembrane potential will result in ion leakage and electrodestruction [8]. Such a condition can lead to a loss of target cells as well as the reduction of cell viability in an isolation device. To prevent these problems, the electric field within a DEP microchamber needs to be carefully adjusted. Besides, the isolation should be completed within a short duration after the sample processing starts. A study conducted by Gascoyne and Shim suggested that the highest field region to which cells are exposed should not be more than 5×10^5 Vm^{-1} and the exposure time to **F**DEP should not be more than 400 s for blood cell separation [6].

1.4. Magnetic Field Strength in the MAP Stage

Similar to **F**DEP, **F**MAP is dependent on the magnetic field generated by the magnetic flux source, which in this study are permanent magnets. The total force exercised on a MAP microfluidic chamber can be calculated by [9]:

$$\mathbf{F} = \int_s (\mathbf{M} \cdot \mathbf{B_o}) d\mathbf{S} \tag{S6}$$

where $\mathbf{B_0}$ is the magnetic field generated by the permanent magnet, while $d\mathbf{S}$ is a vector in the surface normal direction, whose modulus is equal to the area of $d\mathbf{S}$. This expression implies, that the total magnetic force on a MAP microchamber is determined by the surface magnetization (**M**) and the surface orientation of the magnet. More specifically, the magnetic field within the capture region falls off inversely with the square of the distance to the magnet and it can be represented as [10]:

$$\mathbf{B}(y)\,\alpha\,\frac{\mathbf{B_0}}{(S + y)^2} \qquad (S7)$$

where S is the thickness of the substrate, and y represents the distance between the permanent magnet and the channel wall. To enable effective capture distance of the magnetic force, the distance of the permanent magnet from the middle line of the microfluidic channel should not be more than 10 mm [11]. Meanwhile, for face-to-face permanent magnets, the magnet length (L_m) over the inter-magnet gap ratio has to be equal or more than 1 [12]. Aforesaid, enhancing $\mathbf{F_{MAP}}$ by increasing the magnetic field intensity can improve the cell capture rate. To achieve the field strength required for successful targeted cell capture, the magnetic field gradient within the microfluidic channel should not be less than 10 T/m^2 [13].

1.5. Dilution Ratio

As alluded to previously, the massive numbers of blood cells (e.g., 5×10^6 cells in each microliter of blood) will result in overlapping cells within a microchannel. Such a condition is undesirable in this study because it will prevent the device from precisely isolating target cells from a whole blood sample. To circumvent this problem, the blood samples are generally diluted with diluent before proceeding to a benchtop separation process [14]. Dilution reduces the concentration of blood cells per unit volume, thus allowing for rapid detection of certain particles from the dense colonies. The numbers of cells per volume concentration (with units such as cells/mL, cells/L) of diluted blood can be calculated by employing the equation as below [15]:

$$C_1 V_1 = C_2 V_2 \qquad (S8)$$

where C represents the concentration and V is the sample volume. Their subscript indicates the type of solution, in that 1 refers to the whole blood sample and 2 to the diluted blood solution.

Multiple studies have explored the effect of wide ranges of dilution on blood samples [15,16]. A study conducted by Chen et al. [17] found lyses among white blood cells when the dilution ratio of whole blood to saline exceeds 1:11. This statement is in agreement with the result elucidated by Peter et al. [18] in 1964. Their experiment found that blood plasma would undergo a significant change in water and protein concentration, when dilutions are equal or exceeded clinically. Consequently, the blood viscosity will be reduced, followed by increasing size of blood cells, which further leadsa to cell lysis once it exceeds the cell's membrane viscoelasticity. Furthermore, very recently, a research group from Ghent University, Belgium, reported the dilution of whole blood sample greater than 1:10 reduces the Fe isotopic composition within the RBC due to the increase of matrix elements such as Na and K [19]. Such a condition is not favourable in our study as it will reduce the efficiency of MAP as a pre-enrichment stage to separate RBC cells from the blood sample. For the purpose of cell study on a benchtop device, the dilution ratio (whole blood:saline) not more than 1:10, as suggested by Anoshkina et al. [19] is employed. Beyond this point, study has reported the viscosity of these mixtures remains similar to the undiluted blood and no changes are detected among the blood cells.

1.6. Material of the Microfluidic Channel

There are a few factors to be considered when choosing a material for a microfluidic system: such as required function, and degree of integration. Since a microfluidic channel is the basis of building a microchip, the ability of photonic interrogation of the sample is required. Therefore, the material chosen must be transparent to visible light. Besides, such a material must be biocompatible and will not react with the chemical properties of the fluid flowing through it. Furthermore, the material needs to have a high flexibility and versatility during the fabrication process. Notably, a study conducted by Li et al. showed that large capillary forces which are detected within a microfluidic device as a result of integration of fluid movement and detection instrumentation will cause the microchannel wall substrate to swell, crack or dissolve [20]. Such a condition is undesirable as it may drive fluids into unwanted areas of the device, risking contamination of a fluid stream and dislocation of the cells. To overcome this problem as well as to fulfil the application of our device, quartz glass was selected as material for the channel or spacer which serves as the passage for fluid in our computational simulation. Combination of this material with a deformable component such as polydimethylsiloxane (PDMS) can enable integration of microelectrodes and ferromagnets into the channel.

1.7. Fabrication Complexity

Although various microfabrication techniques are employed to process and fabricate a gasket, the increased complexity of the microfluidic system can result in higher cost. This is because different channel depths and dimensions require a series of fabrication procedures which involve sophisticated technologies. In this context, a microfluidic channel with a rectangular cross-section was selected in our design due to the ease of fabrication. To prevent the microfluidic channel from collapsing during the fabrication process, its aspect ratio (height:width) should not be lower than 1:10 [21]. Besides, the minimum allowed width of the channel should be limited to approximately 0.25 mm to allow a sufficient margin for bonding [1].

1.8. Uniformity of Flow

Finally, in our application, it was necessary to make sure that the flow velocity is as uniform as possible within a microfluidic channel. As a consequence of inserting cell suspension through the inlet, the flowing of non-uniform fluid across the channel resulted in sedimentation of cells at a particular point within the microfluidic channel [22,23]. Such a condition is undesirable for cell analysis because it reduces the sensitivity of the MAP or DEP force received by each cell [24]. Thus, to ensure uniform loading capacity for a given chamber size, it is crucial that the whole area reaches saturation at the same time. In this case, cross-section of the microfluidic channel should be increased and this is further discussed later in the paper.

2. Design Development

The control of fluid flow and forces distribution within a microfluidic device are highly influential for the deposition and separation of cells within the chamber. To achieve a desirable output, the variables which affect the performance of our proposed MAP stage need to be optimized and evaluated before integrating it with a DEP stage. These include permanent magnet orientation, magnetic field gradient across a ferromagnetic track, hydrodynamic mechanism, separation efficiency, and dilution ratio. The evaluation is accomplished with computational simulation whereby algorithms are used to solve and analyse the problem under the experimental condition.

2.1. Permanent Magnet Orientation

As mentioned beforehand, the permanent magnet configuration influences the magnetic force generated within a MAP microchamber. To obtain the desirable cell separating configuration in our

proposed MAP stage, it is important to employ a correct magnet orientation. For this purpose, the effects of various permanent magnet orientations on magnetic force distribution within a microfluidic channel were examined and compared. A single magnet configuration, two magnets placed in attraction, and two magnets in repulsion, were considered respectively as depicted in Figure S1. For instance, Figure S1a illustrates the single permanent magnet configuration. A permanent magnet was aligned in a way whereby the direction of the field was parallel with the direction of the fluid flow within the microchannel. Meanwhile, for face-to-face magnet configuration, the microchannel was surrounded by two permanent magnets. These magnets were placed in north-to-south (attractive) and north-to-north (repulsive) orientations. They are shown in Figure S1b,c, respectively. In this study, the distance of the permanent magnet from the microchannel wall was fixed at 5 mm, which was half of the maximum allowed value for all configurations. Nevertheless, to ease the fabrication process as well as to balance the magnetic forces, permanent magnets used in our study had axial symmetry.
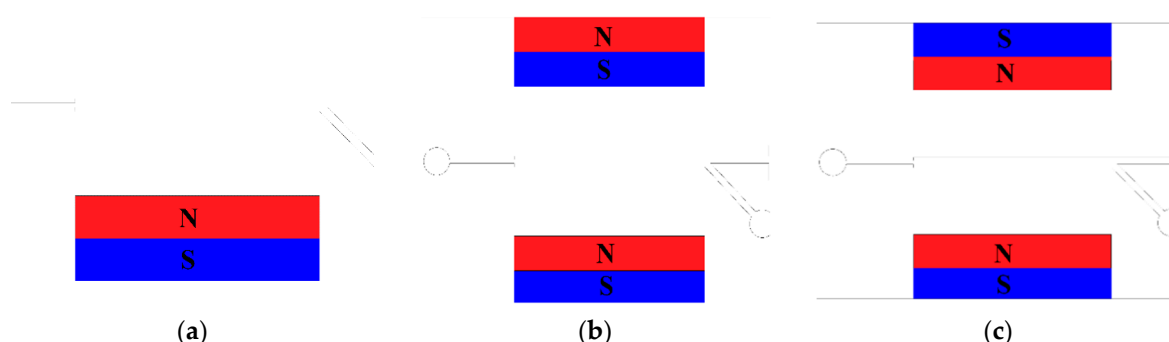
Figure S1. Schematic illustration of the microfluidic channel with its magnet: (**a**) Conventional imbedded permanent magnet configuration; Face-to-face permanent magnet in (**b**) attractive and (**c**) repulsive configuration.

2.2. Measurement of the Magnetic Field Gradient across the Ferromagnetic Track

Notably, the used of a ferromagnetic track coupled with permanent magnet can concentrate the magnetic field over the confined space of a microfluidic channel, thus producing a force to efficiently separate targeted cells under a continuous flow. However, the majority of the available ferromagnetic track designs were limited in their effectiveness in cell separation for a microfluidic channel which was less than or equal to 100 μm wide [25]. As a channel dimension contributed to our device throughput, the range of width used for the MAP microchamber in a previous study was too small for our system. Such a condition resulted in a longer time needed to process one sample. To solve this problem, a ferromagnetic track was proposed to be embedded in the middle of the MAP microchamber. The design is showed in Figure S2. A magnetic field generated within the MAP chamber with the presence of ferromagnetic track was examined in this study.
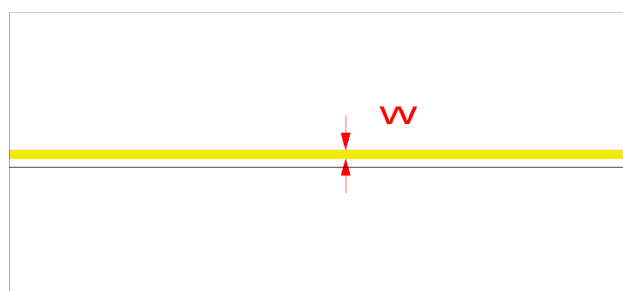
Figure S2. Schematic illustration of ferromagnetic track (represented with yellow segment) within a MAP microchamber.

A study conducted by Chen et al. [26] reported a correlation between the cross-sectional area of a ferromagnetic track and the magnetic field. An equation was formulated based on the experimental observation, such that:

$$B_0 = \frac{9\mu_0 \eta}{R_c^2 \Delta\chi_c} \times \frac{H \cdot FR}{W \cdot L} \times \frac{1}{(S + W)^{-4} - S^{-4}} \tag{S9}$$

where FR represents flow rate. W, H, and L refer to the width, height, and length of the microfluidic channel, respectively. Meanwhile, S is the cross sectional area of the ferromagnetic track. Since both the length and height of the magnet track were accommodated according to those of the MAP microchamber, this equation impliesthat the magnetic field is inversely proportional to the width of the magnetic track. In this case, a very strong field was created over small distances and small displacements on the scale of the ferromagnetic track. To obtain an effective F_{MAP} in our proposed microfluidic architecture, the width of the ferromagnetic track was fixed at the allowed minimum fabrication value, which was 250 μm.

2.3. Hydrodynamic Mechanism

Apart from magnetic field and electric field distribution, it should be noted that the effectiveness of our proposed MAP-DEP microdevice is dependent on the hydrodynamic force subjected within the microsystem. To produce a particular output response at the drain-outlet ports, the flow requirements as mentioned earlier in Section 1 have to be fulfilled. Therefore, velocity profile and dynamic pressure generated within a proposed channel topology were examined. Notably, the hydrodynamic mechanism is dependent on channel geometry. In this context, flow rate can be optimized by tailoring the proposed geometry.

2.4. Separation Efficiency

For a benchtop CTC detection device, it is necessary to analyse and optimise the devices' performance before they are employed in an experimental setup. To evaluate the proposed isolation technology, the key performance metric which was capture efficiency (or recovery rate) was measured in our numerical study. Note that capture efficiency refers to the fraction of captured target cells relative to the total captured cells. It is usually expressed as a percentage (%). This measurement is important in accessing the total of target cells which have been lost in the isolation process. A high capture efficiency represents less cell losses and thus provides clinician accurate information about the amount of target cells discovered from a given sample [27].

In our study, an early-stage assessment of MAP operational performance was conducted to investigate its recovery metric as well as the cell separation dynamics. Following this, the analysis of our finalised integrated platform's functionality was implemented to ensure compatibility of the proposed MAP stage with the DEP application.

2.5. Dilution Ratio

The majority of microfluidic techniques demonstrate a dramatic reduction in capture efficiency when a whole blood sample is employed. Therefore, the blood sample is typically diluted with saline solution before it is injected into an isolation microfluidic device. However, it should be noted that a dilution would reduce the concentration of cells carried by the fluid flow toward the MAP and DEP chamber. Under a constant velocity field, a sample with high dilution ratio will result in a lower throughput in contrast to the low-dilution-ratio sample [28]. To gain insight on the correlation between dilution ratio on both separation efficiency and the device's throughput, particle tracing simulation was conducted. As our proposed MAP platform handled highly concentrated cell samples, the evaluation was mainly focused on this stage. In favour of this simulation, multiple dilution ratio proportions (whole blood: saline) such as 1:0,1:1, 1:2, 1:3, 1:4, 1:5, 1:6, 1:7, 1:8, 1:9, and 1:10 were used with a constant concentration of saline. The target cells obtained from a sample with the corresponding dilution ratio across the optimised flow velocity were

observed. Finally, a dilution ratio which provided the best discovery rate without compromising both device efficiency and throughput was deduced in this study.

3. Proposed Microfluidic Architecture

Figure S3 presents a structure of our proposed MAP-DEP based microfluidic interface. The overall design was configured in a way similar to that of the standard microscopic slide format, as such 78 mm long and 25 mm wide. This enabled the entire device on a small glass slide to be placed on the size of a human palm, and therefore fulfil the fundamental need of a lab-on-a-chip.
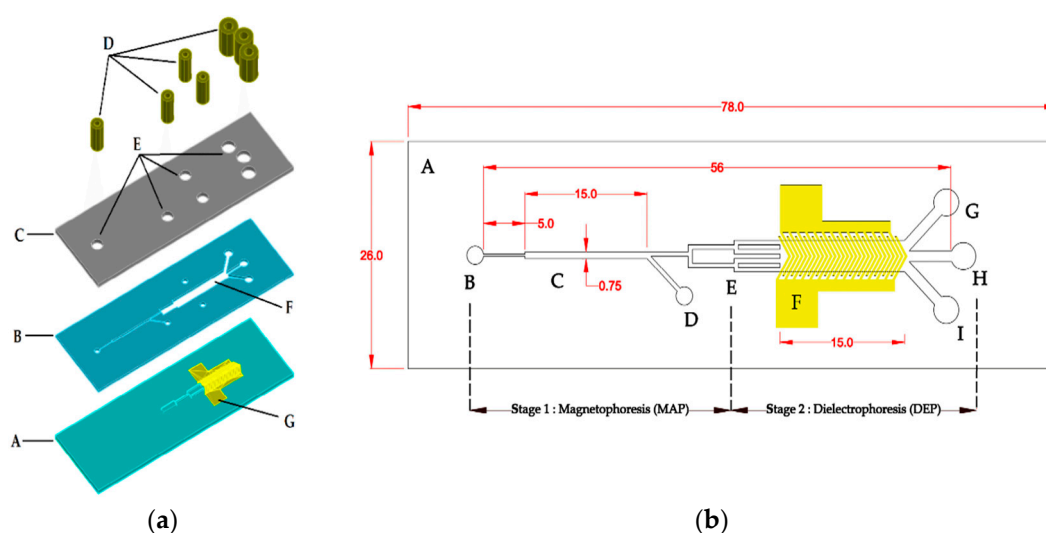

(**a**)   (**b**)

Figure S3. Proposed MAP-DEP based microfluidic platform: (**a**) The schematic shows assembly components spreading out of the microfluidic device (see Table S1 for description); (**b**) Mask design for microfluidic channel and the electroplated microelectrode structure (see Table S2 for description).

Table S1. Component description for Figure S3a.

	Components	Material	Function
A	Bottom glass die with metal deposition	Polydimethylsiloxane (PDMS)	Is bonded via plasma treatment to provide a miniaturized separation platform
B	Spacer	Glass	
C	Cover slip	Indium tin oxide	Put on top of spacer to keep the cell sample intact during the isolation process
D	Rubber O-ring	-	To hold capillary tubes (which interface the macroscale fluid delivery system to microscale to a microscale separation system) firmly in place
E	Port interconnection	-	To provide inlet and outlet ports for microfluidic injection and ejection
F	Separation chamber/microfluidic channel	-	To direct the fluid flow
G	Electroplated microelectrode	Titanium dioxide (To_2O)	To generate electric field

Table S2. Component label for Figure S3b.

	Component
A	Glass substrate
B	Inlet reservoir
C	MAP microchamber
D	Outlet reservoir #1
E	Tree-network bifurcation
F	DEP microelectrode
G	Outlet reservoir #2
H	Outlet reservoir #3
I	Outlet reservoir #4

As depicted in Figure S3a, the microfluidic device consisted of three important layers: bottom glass die, spacer, and cover slip. In order to ease our computational study, the glass cover slip was bonded to serve as the substrate or the "capture plane", with a negligible thickness. A close-up view of our proposed microfluidic channel employed for computational study is illustrated in Figure S3b.

In this figure, the proposed microfluidic channel supported two microseparation processes, such that MAP separation in stage 1 was followed by DEP separation in stage 2. For the MAP stage, permanent magnets which were made of neodymium–iron–boron (Ne-Fe-B) featuring magnetic flux densities of 500 mT, were employed to generate the magnetic field over the MAP chamber. Meanwhile, in the DEP stage, an array of interdigitated divergent-shape microelectrodes were embedded at the bottom of the chamber. A metal contact, as presented in the figure above, connected them with an external sinusoidal electric potential to create an electric field for cell capture. Although the use of planar electrodes were able to increase the surface area for reaction, a study conducted by Kadri [28] showed that cells were not homogeneously distributed over the electrodes. Such a condition will hinder our integrated micro-device from achieving its optimal performance. To ensure uniform loading capacity for a given chamber size, a tree-network bifurcation from our previous study [29] was implemented into this proposed design (see Figure S3b). The detailed architecture of the design was further discussed in the main text Section 4. When a suspension of blood sample spiked with CTCs was simulated to flow into this system, the cells entered the first stage through an inlet. A MAP force was exhibited on these blood cells as they passed through the MAP microchamber. In the end of the MAP stage, red blood cells (RBCs) were removed and collected in outlet 1. Concurrently, the enriched nucleated cells such as white blood cells (WBCs) and CTCs were directed into the DEP stage to undergo DEP force. This leads to a separation of CTCs from other nucleated blood cells. Depending on the dielectric properties of both CTCs and WBCs, they were led toward their designated collection outlet in the end of the DEP stage.

As alluded to in the previous section, the dimension of the microfluidic channel is correlated with the distribution of the electric, magnetic, and hydrodynamic forces. Therefore, these parameters should be incorporated into the course of this study to help developing a successful microchip device based on a force balance equation between DEP, MAP, and the hydrodynamic force. It has been known that the electric field distribution within the channel is decayed significantly at a height greater than 0.5 mm [1]. To achieve optimal sample processing volume as well as to accommodate the DEP stage requirement, the height of the entire microfluidic channel was therefore fixed at 0.5 mm. As shown in Figure S3b, the entrance length was set at 5 mm. This is because a consistent flow profile was found to be quickly developed at this linear extent [30]. Meanwhile, the length of both the MAP and DEP microchambers were assigned as 15 mm respectively to accomplish the terms of optimum sample volume.

Since both length and height of the microchannel were fixed, subsequently, the channel width directly influenced performance of our integrated device. In this case, a width of 0.75 mm was employed for the MAP microchamber of Stage 1. This is the allowed maximum value for an effective magnetic field to be distributed within the channel, providing that a permanent magnet is located on the side of MAP microchamber [31]. Meanwhile, in stage 2, the width of the DEP microchamber was regulated according to the output channel width from MAP stage (see Figure S3b). Notably, the width of the MAP output channel was determined in dependence of the cells' positions in the gradient. Thus, these dimensions were decided based on the result of cell trajectory analysis in this study. Nevertheless, a microfluidic structure with height-to-width aspect ratio below 1:10 (height:width) is prone to collapse. To avoid this issue, the suggested width of the DEP chamber should not be more than 5 mm [32].

4. Theory and Model

The capture efficiency of our proposed integrated MAP-DEP platform was predicted using a computational model (with COMSOL Multiphysics) that focused on the magnetic and

hydrodynamic forces as well as particle-fluid interactions. This model solved the partial differential equations that govern each physical process with the Lagrangian-Eulerian CFD-based numerical scheme, whereby the Lagrangian analysis was used to track the motion of cells within the proposed MAP stage, while an Eulerian-based CFD analysis was employed to solve the Navier Stokes momentum equation. Although the model is for proof-of-concept purposes, it should be noted that the MAP is an experimentally validated theory that has been employed for several decades to capture RBCs in the presence of a magnetic field. As part of our progress, the cell trajectory and capture performance within our proposed system was analysed computationally by assigning the data which were derived from the expression of the magnetic force and Navier Stokes momentum equation for the solver. The model is described in more detail as following:

4.1. Magnetic Field

The magnetic field module was used to model the force in the MAP stage. In the magnetostatic simulation, the magnetic field with no current module was loaded. The heart of formulae for the analysis of the magnetic system is the Maxwell equation. The equation is written as below:

$$\nabla \times (\mu_0^{-1}\mu_r^{-1}\nabla \times \mathbf{A} - \mathbf{B_r}) - \boldsymbol{J}^e + \sigma\frac{\Delta V}{L} = 0 \tag{S10}$$

This formulation is applied across the quadratic Lagrange elements, where σ is the conductivity, μ_0 is the magnetic permeability in a vacuum, μ_r is the relative magnetic permeability, $\mathbf{A}$ is the magnetic vector potential, $\boldsymbol{J}^e$ is an externally generated magnetic current density, B_r is the remanent magnetic flux density, ∇V is the potential difference, and L is the distance. Once the global governing equations were applied, the constitutive relation of the permanent magnet, as well as the MAP microfluidic chamber were defined.

In the subdomain setting, the permanent magnet was modelled as a body with magnetization uniformly directed toward the MAP microchamber. Its constitutive relation is designated as:

$$\mathbf{B} = \mu_0\mu_r\mathbf{H} + \mathbf{B_r} \tag{S11}$$

The magnetic field was defined by the remanent flux density of 500 mT. The magnetic permeability of the simulated permanent magnet was provided according to standard manufacturer's datasheets such that μ_r is 1.05 [33]. Meanwhile, for the MAP microchamber, the constitutive relation is denoted as:

$$\mathbf{B} = \mu_0(\mathbf{H} + \mathbf{M}) \tag{S12}$$

The resulting magnetization within the microchamber, **M**, was dependent on the magnetic susceptibility volume of blood. It should be noted that a soft element of NiFe was imbedded within the MAP microchamber to enhance the magnetic field. It can be modelled by imposing the magnetization response as arbitrary **M** (**H**) relation in the subdomain settings.

Notably, the magnetic analysis needs a larger (open) domain because the field extends to infinity. A large number of computational nodes were therefore required to achieve accurate magnetic force values, which resulted in an increase in computation time and inhibited large-scale parametric analysis. To ensure a proper distribution of the magnetic field in the surrounding space, a closed-form magnetic analysis was used. An environment was drawn enfolding the whole device with few boundary condition sas below:

i   A symmetry boundary is set on the *xz* plane in accordance to *y* = 0.25, along the midline of the microchamber.

ii   The boundary conditions on the interior boundaries are set by default to continuity, as such:

$$\boldsymbol{n} \times (\mathbf{H_1} - \mathbf{H_2}) = \mathbf{0} \tag{S13}$$

where H indicates a magnetic field. Meanwhile, magnetic insulation was set on the external boundaries of the environment, except for the symmetry point in which a zero potential condition is implied. Such a setting is able to enhance computational power since the *y* = 0.25

plane is characterized by either magnetic field maxima or minima for symmetry reasons while other external boundaries which are drawn further from the field source would have a null magnetic field.

4.2. Electric Field

The electric current interface was used to model the DEP stage, whereby the magnetic-inductive effects were neglected in this stage and only resistive-conductive and electric-capacitive effects were accounted for. In this simulation, the electric potential in the microchannel was governed by Laplace's equation of continuity such that:

$$-\nabla \cdot ((\sigma + j\omega\varepsilon_r\varepsilon_o)\nabla\varphi) = 0 \qquad (S14)$$

where σ represents the electrical conductivity of the cell, ω is the angular frequency of the driving field, $\emptyset$ is the electric potential, ε_r is the relative permittivity of the medium, and ε_o is the relative permeability of the vacuum. By solving this equation, the electric field generated by the microelectrode, **E** and the displacement of currents, **D** can be obtained, as such:

$$\mathbf{E} = \nabla\varphi \qquad (S15)$$

$$\mathbf{D} = \varepsilon_r\varepsilon_o\mathbf{E} \qquad (S16)$$

A few boundary conditions are set as follows:

i. Electrodes are assumed to be isopotential, thus their thickness and height is neglected in electric field simulation.
ii. The voltage is defined as a sine wave at a particular frequency, whereby electric potentials of +15 V and −15 V are assigned across alternating electrodes embedded within the microchannel. A non-uniform electric field is established either vertically or laterally, depending on the microelectrode configuration.
iii. The other external boundaries are set to be electrical insulated, such that:

$$\boldsymbol{n} \cdot \mathbf{J} = 0 \qquad (S17)$$

where **J** is the current density. However, for the boundaries that representing the electrode gaps, imposing an insulation condition will result in a mathematical singularity due to the competing Neumann and Dirichlet conditions. To solve this problem, the Neumann condition inside the gaps is changed by a Dirichlet condition, imposing the voltage to linearly vary between the values assumed at the two subsequent electrodes.
iv. For the interfaces between the cell surface and the medium, the continuity of the electric displacement (**D**), electric field (**E**), and current density (**J**) are designated according to:

$$\boldsymbol{n} \cdot (\mathbf{D_1} - \mathbf{D_2}) = \boldsymbol{\rho_s} \qquad (S18)$$

$$\boldsymbol{n} \cdot (\mathbf{E_1} - \mathbf{E_2}) = 0 \qquad (S19)$$

$$\boldsymbol{n} \cdot (\mathbf{J_1} - \mathbf{J_2}) = 0 \qquad (S20)$$

where $\boldsymbol{\rho_s}$ is the surface charge density.

4.3. Fluid Flow

To direct the fluid flow into the proposed micro-device, the incompressible Navier-Stokes module was loaded. Its equation is written as:

$$\rho\frac{\partial\boldsymbol{u}}{\partial t} - \nabla \cdot \sigma + \rho\mathbf{u} \cdot \nabla\mathbf{u} = \mathbf{F} \qquad (S21)$$

In this equation, **u** is the velocity vector containing u and v components along the *x*, *y*, and *z* direction. Meanwhile, ρ is the fluid's density, p is the flow's pressure, and σ represents the total stress tensor of Newtonian fluid which consists of pressure stress and viscous stress. σ can be further expanded into:

$$\sigma = -p\mathbf{I} + \eta\,(\nabla\mathbf{u} + (\nabla\mathbf{u})^\mathrm{T}) \tag{S22}$$

where **I** is the identity matrix, and η represents the dynamic viscosity of the fluid. To fully describe the fluid flow, a statement of the conservation of mass is necessary. Considering both ρ and η are constant throughout the fluid, a mass continuity equation can be formulated such that:

$$\nabla^2\mathbf{u} = \nabla p \tag{S23}$$

$$\nabla \cdot \mathbf{u} = 0 \tag{S24}$$

It is noteworthy that only the fluidic channel is active in this mode whereby its subdomain settings are internally specified for blood. The inlet and outlet ports of the microchannel were defined at the beginning of the MAP and end DEP stage, respectively. The boundary conditions for Incompressible Navier-Stokes are summarised as following:

i.   No-slip boundary conditions are used at the wall whereby the velocity generated at the channel wall is zero.

$$\boldsymbol{u} = 0 \tag{S25}$$

ii. The inlet is provided with an inflow boundary condition of velocity. The unidirectional pressure-driven flow with a parabolic velocity profile at the channel inlet is given by:

$$u(y) = \boldsymbol{x}\frac{\Delta P}{2\mu}y(\mathrm{H} - y) \tag{S26}$$

where ΔP is the axial pressure gradient, H is the microchannel height, and y is the direction of the cell height's coordination (with $y = 0$ at the cell floor).

iii. The outlet boundary condition is considered with the mass flux adjusted to satisfy the continuity Equation (S14), such that the direction of mass flow is principally determined by the pressure inside the outlet boundary. Therefore, the pressure generated on the outlet, which served as a reference pressure for the incompressible flow is equal to zero.

4.4. Particle Trajectory

To monitor the device functionality, the cell trajectory within both the MAP and DEP stages was computed using the Particle Tracing Module. This module calculated the trajectory of cells, which were suspended in the blood sample, as they moved through our proposed device by solving the equation of motion for each set of cells. The equation is governed by Newton's second law such that:

$$\mathrm{m}\frac{d\boldsymbol{v}}{dt} = \mathbf{F}_c \tag{S27}$$

where m is the mass of cells, v is the cell velocity, and $\mathbf{F}_c$ is the total force experienced by the cells. By considering a cell to be located at a position $x(t)$ in a fluid, its position vector can be written as:

$$\frac{dX(t)}{dt} = \boldsymbol{v} \tag{S28}$$

whereby the velocity of the particle, v can be obtained by integrating the Equation (S19). Taking the initial condition for the particle velocity as stationary and located at position vector $x(t_0)$, the equation for the position vector can be rewritten as:

$$x(t) = (\frac{\mathbf{F}_c}{\mathrm{m}})t^2 + v_o t + x_o \tag{S29}$$

Via Equation (S20), the cell trajectory can be traced by iteratively updating the position according to the flow field and the forces that are imposed on the cell.

Notably, the resulting force acting on the cells is composed of four main components: hydrodynamic force ($\mathbf{F_{HYD}}$), which is caused by the resistance to the motion of a cell; MAP force ($\mathbf{F_{MAP}}$), which is caused by the non-uniform magnetic field; DEP force ($\mathbf{F_{DEP}}$), which is due to

non-uniform electric field, and Brownian force, which is responsible for the random motion of cells resulting from the collisions with the fast-move molecules of the fluid. The equalities of these forces can be expressed as following:

$$\mathbf{F} = \mathbf{F_{MAP}} + \mathbf{F_{DEP}} + \mathbf{F_{HYD}} + \xi \sqrt{\frac{12\pi k_b \mu T r_c}{\Delta t}} \tag{S30}$$

where ξ is a unit-variance-independent Gaussian random numbers and k_b refers to the Boltzmann constant (1.38065 × 10⁻²³ J/K). In this equation, the formulation for the first three terms has been discussed in our paper. Meanwhile, for the Brownian force (which is represented by the forth term), its amplitude is dependent on the fluid temperature (T) and the radius of the cell (r_c). As the equation for this force vector was already embedded in the module, the theoretical trajectory of cells was computed automatically according to the post-processing data of magnetic field, electric field, and fluid flow, respectively.

5. Additional Results

5.1. Gradient of Magnetic Flux Density for a Single Permanent Magnet

Notably, the operative of magnetic force in a MAP system is determined primarily by two factors: (1) gradient of magnetic flux density ($\nabla \boldsymbol{B}^2$); and (2) the volumetric magnetic susceptibility difference ($\Delta \chi$) between the cells and the surrounding buffered fluid medium. Due to the magnetic susceptibility of blood cell being on the order of 10^{-6} to 10^{-7}, this parameter does not impact the force calculation within the proposed MAP system. Therefore, the MAP force exerted on cells was mainly dependent on $\nabla \boldsymbol{B}^2$. As alluded to in Section 3.2 of our article, the distribution of $\nabla \boldsymbol{B}^2$ should not be less than 10T/m² for a MAP cell separation device. To ensure the optimum MAP force obtained for cell separation, $\nabla \boldsymbol{B}^2$ within the microchannel of the selected magnet configuration (which is a single permanent magnet in our case) was investigated. An expression for $\nabla \boldsymbol{B}^2$ can be expanded in explicit form to yield:

$$\nabla \boldsymbol{B}^2 = (\vec{B} \cdot \nabla)\vec{B} = \begin{bmatrix} B_x \dfrac{\partial B_x}{dx} + B_y \dfrac{\partial B_x}{dy} + B_z \dfrac{\partial B_x}{dz} \\[2mm] B_x \dfrac{\partial B_y}{dx} + B_y \dfrac{\partial B_y}{dy} + B_z \dfrac{\partial B_y}{dz} \\[2mm] B_x \dfrac{\partial B_z}{dx} + B_y \dfrac{\partial B_z}{dy} + B_z \dfrac{\partial B_z}{dz} \end{bmatrix} \tag{S31}$$

By assuming the single permanent magnet which was located at the side of microchannel was infinitely long in *x*-direction, Equation (S21) can be simplified whereby the spatial derivatives of the *x* component are written as:

$$\frac{\partial \vec{B}}{\partial x} = 0 \leftrightarrow \left\{ \frac{\partial B_x}{dx} = 0, \frac{\partial B_y}{dx} = 0, \frac{\partial B_z}{dx} = 0 \right\} \tag{S32}$$

As mentioned previously, the flow will be established throughout our proposed continuous cell sorting system in the horizontal direction (*x*-axis). As B_y was directed across the channel width, it induced the magnetic velocity that was superimposed with cell separation in the MAP stage. An iso-value of $\nabla \boldsymbol{B}^2$ in the y-direction can be provided by:

$$\nabla \boldsymbol{B}^2 = \left[B_y \frac{\partial B_y}{dy} + B_z \frac{\partial B_y}{dz} \right] \tag{S33}$$

In Figure S4, the graph shows that the derivative of the magnetic field is reduced with the distance from the permanent magnet, wherein the difference between the highest and lowest value of $\nabla \boldsymbol{B}^2$ was 3.6 T/m². However, the gradient of the magnetic field obtained from this simulation was 9.4 T/m². Such a condition does not fulfil the design requirement which states that the magnetic field gradient exacted on the cells within the microchamber has to be more than 10 T/m² (refer to Section 1). To optimize the $\nabla \boldsymbol{B}^2$, a soft magnetic element was integrated in our proposed MAP stage.

Graph of magnetic field gradient across the width of MAP microchamber
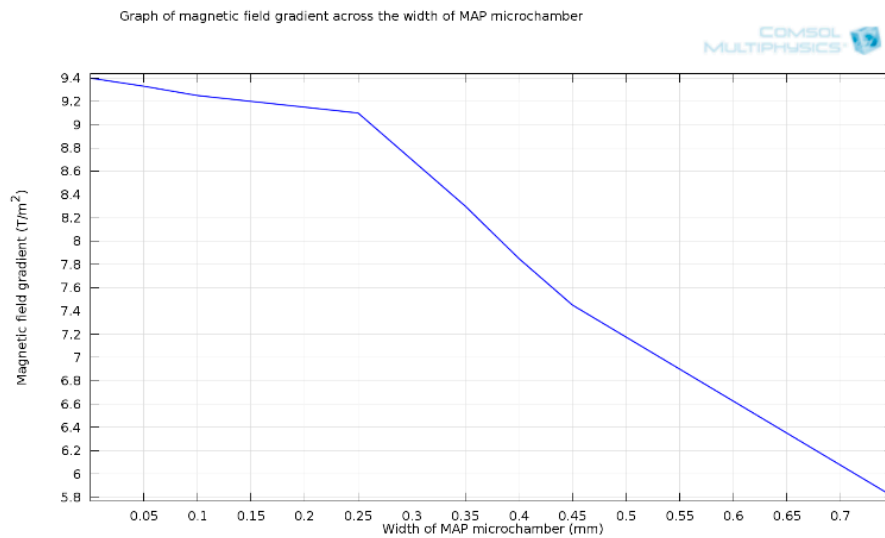

Figure S4. Analysis of ∇B^2 across the width of the MAP microchamber.

5.2. Inlet Velocity

For a preliminary evaluation of flow profile within a channel, the inlet flow velocity boundary condition was determined based on the desired velocity field within a MAP microchamber. As alluded to in Section 1.2, a velocity flow generated within the MAP chamber should fulfil the range as stated in Equation (5) to ensure that all cells reach their equilibrium positions under $\mathbf{F}_{HDY}$ and $\mathbf{F}_{MAP}$. In pursuance of higher throughput, the optimized velocity field was adapted to be not more than the maximum flow parameter. Equation (5) can thereby be rewritten as:

$$v_{M\_opt} < \frac{l\,\mu_f\,(\chi_p - \chi_m)\,V_c\frac{\partial H_{ext}}{\partial y}^2}{4\pi\eta\,wR} \tag{S34}$$

In this equation, the l and w which refer to the length and width of the MAP microchamber are 15 mm and 0.25 mm, respectively. Meanwhile, $\frac{\partial H_{ext}}{\partial y}$ can be defined through a Matlab plot in Figure 10, whereby an average value of 49 T/m² is employed for this calculation. It was known that RBC was the targeted cell in our proposed MAP stage. To achieve the optimum flow velocity without compromising its recovery rate, Equation (S22) was determined based on the RBC properties (see Table 1 in the main text). By substituting the values into Equation (S22), an approximate velocity flow within the MAP chamber was calculated and represented as below:

$$v_{M\_opt} < \frac{l\,\mu_f\,(\chi_p - \chi_m)\,V_c\frac{\partial H_{ext}}{\partial y}^2}{4\pi\eta\,wR} < \frac{2.44 \times 10^{-11}}{5.03 \times 10^{-11}} < 97 \times 10^{-3}\ \text{m/s}$$

Note that a study conducted by Emerson et al. [34] showed that the volumetric flow rate is halved at each bifurcation, such that the mean velocities the of n-folded network can be written as:

$$\frac{V_n}{V_{in}} = 2^{-n}\frac{A_0}{A_n} \tag{S35}$$

where A_0 and A_n represents the cross section of an inlet and its drain channels. To obtain a flow velocity of 90 mm/s for our proposed design, the inlet velocity boundary condition for 0.25 mm ($V_{0.25in}$) and 0.75 mm ($V_{0.75in}$) width inlet was fixed at 0.2 m/s and 60 mm/s, respectively. The calculations are shown below:

$$\frac{90\frac{\text{mm}}{\text{s}}}{V_{0.25in}} = 2^{-1}\frac{0.25\text{mm} \times 0.5\text{mm}}{0.25\text{mm} \times 0.5\text{mm}}$$

$$V_{0.25in} = \underline{0.2\ \text{m/s}}$$

$$\frac{90\,\frac{mm}{s}}{v_{in}} = 2^{-1}\frac{0.75mm \times 0.5mm}{0.25mm \times 0.5mm}$$
$$V_{0.75in} = \underline{60\ mm/s}$$

6. Future Works

The result portrayed by our computational study has offered a few interesting directions for future works. There are a few significant improvement which can be carried out to validate and brush up the current developed microfluidic platforms.

6.1. Experiment Setup

The recovery rate of target cells for the proposed integrated microfluidic platform is the main concern in this study. A major factor that impacts this parameter, such as loading concentration, needs to be investigated and compared with simulation results. The experimental work can be carried out by first labelling the target cells with fluorescent beads. When the cell sample is injected into the microfluidic platform, the trajectory of cells along the chamber can be measured by a charged-coupled-device CCD-type camera to obtain the real time velocity field as well as the deviation route.

Notably, maintenance of cell viability is an imperative feature of a label-free cell separation procedure because the captured living cells are needed for downstream phenotypic and genotypic analyses. A systemic investigation of the electrical and magnetic field effects that may influence cell integrity and viability should be included in the experimental study. The viability test can be done by dye exclusion techniques where cells are incubated with a dilute solution of dye which only enters dead cells.

6.2. Device Fabrication

The main challenge of our proposed device fabrication is the technique used to embed the ferromagnetic track in the middle of the microfluidic channel. One potential method for fabrication would be layer-by-layer approach, wherein the ferromagnetic element is formed via a sequence of spin coating, patterning, etching, deposition, and planarization followed by the removal of sacrificial material to form the flow channel. Some challenges with this approach include the time required for the precision in patterning and depositing a ferromagnetic track, the potential for detrimental residual stress in the system, and the ability to etch a flow channel with uniform cross-sectional dimensions with the elements in place. An alternative method would be to use 3D printing to form the system and insert the ferromagnetic elements relatively during fabrication.

References

1. Saliterman, S.S. *Fundamentals of Biomems and Medical Microdevices*; Wiley Interscience: Washington, DC, USA, 2006.
2. Moon, H.S.; Kwon, K.; Kim, S.I.; Han, H.; Sohn, J.; Lee, S.; Jung, H.I. Continuous separation of breast cancer cells from blood samples using multi-orifice flow fractionation (moff) and dielectrophoresis (dep). *Lab Chip* **2011**, *11*, 1118–1125.
3. Huang, C.-T.; Amstislavskaya, T.G.; Chen, G.-H.; Chang, H.-H.; Chen, Y.-H.; Jen, C.-P. Selectively concentrating cervical carconoma cells from rare blood cells utilizing dielectrophoresis with circular ito electrodes in stepping electric fields. *J. Med. Biol. Eng.* **2012**, *33*, 51–59.
4. Chawla, R. *Practical Clinical Biochemistry: Methods and Interpretations*, 4th ed.; JP Medical Ltd.: Philadephia, PA, USA, 2014.
5. Lee, A.M.; Tormoen, G.W.; Kanso, E.; McCarty, O.J.; Newton, P.K. Modeling and simulation of procoagulant circulating tumor cells in flow. *Front. Oncol.* **2012**, *2*, 108.
6. Gascoyne, P.R.C.; Shim, S. Isolation of circulating tumor cells by dielectrophoresis. *Cancers* **2014**, *6*, 545–579.

7.	Dimitrov, D.S. Electroporation and electrofusion of membranes. In *Handbook of Biological Physics*; Liposky, R., Sackmann, E., Eds.; Elsevier Science B.V: San Diego, CA, USA, 1995; Volume 1.

8.	Toner, M.; Irimia, D. Blood-on-a-chip. *Annu. Rev. Biomed. Eng.* **2005**, *7*, 77–103.

9.	Furiani, E.P. Magnetophoretic separation of blood cells at microscale. *J. Appl. Phys.* **2007**, *40*, 1313.

10.	Gassner, A.L.; Abonnenc, M.; Chen, H.X.; Morandini, J.; Josserand, J.; Rossier, J.S.; Busnel, J.M.; Girault, H.H. Magnetic forces produced by rectangular permanent magnets in static microsystems. *Lab Chip* **2009**, *9*, 2356–2363.

11.	Porcher, P. Elemental rare earths: Magnetic structure and resistance, correlation of. In *Concise Encyclopedia of Magnetic and Superconducting Materials*; Buschow, K.H.J., Ed.; Elsevier: Oxford, UK, 2005; pp. 156–164.

12.	Zheng, S.; Lin, H.K.; Lu, B.; Williams, A.; Datar, R.; Cote, R.J.; Tai, Y.C. 3D microfilter device for viable circulating tumor cell (CTC) enrichment from blood. *Biomed. Microdevices* **2011**, *13*, 203–213.

13.	Chen, P.; Huang, Y.Y.; Hoshino, K.; Zhang, J.X. Microscale magnetic field modulation for enhanced capture and distribution of rare circulating tumor cells. *Sci. Rep.* **2015**, *5*, 8745.

14.	Gaw, R.L.; Cornish, B.H.; Thosmas, B.J. Comparison of a theoretical impedance model with experimental measurements of pulsatile blood flow. In Proceedings of the 13th International Conference on Electrical Bioimpedance and 8th Conference on Electrical Impedance Tomography 2007, Graz, Austria, 29 August–2 September 2007; pp. 32–35.

15.	Ninivaggi, M.; Feijge, M.A.; Baaten, C.C.F.M.J.; Kuiper, G.J.A.J.M.; Marcus, M.A.; ten Cate, H; van der Meijden, P.E. Additive roles of platelets and fibrinogen in whole-blood fibrin clot formation upon dilution as assessed by thromboelastometry. *Thrombosis Haemostasis* **2014**, *111*, 447–457.

16.	Mylotte, J.M.; Tayara, A. Blood cultures: Clinical aspects and controversies. *Eur. J. Clin. Microbiol. Infectious Dis.* **2000**, *19*, 157–163.

17.	Chen, X.; Cui, D.; Jian, C. Microfluidic devices targeting blood cell lysis. In *On-Chip Pretreatment of Whole Blood by Using Mems Technology*; Xing, C., Ed.; Bentham ebook: Dubai, UAE, 2012.

18.	Peter, W.R.; Eleanor, L. Hemodilution, tonicity and blood viscosity. *J. Clin. Investig.* **1964**, *43*, 2214–2227.

19.	Anoshkina, Y.; Costas-Rodriguez, M.; Vanhaecke, F. High-precision fe isotopic analysis of whole blood for biomedical purposes without prior isolation of the target element. *J. Anal. Atomic Spectrom.* **2015**, *30*, 1816–1821.

20.	Li, M.; Li, W.H.; Zhang, J.; Alici, G.; Wen, W. A review of microfabrication techniques and dielectrophoretic microdevices for particle manipulation and separation. *J. Phys. D Appl. Phys.* **2014**, *47*, 063001.

21.	Saias, L.; Autebert, J.; Malaquin, L.; Viovy, J.-L. Design, modeling and characterization of microfluidic architectures for high flow rate, small footprint microfluidic systems. *Lab Chip* **2011**, *11*, 822.

22.	Millet, L.J.; Park, K.; Watkins, N.N.; Hsia, K.J.; Bashir, R. Separating beads and cells in multi-channel microfluidic devices using dielectrophoresis and laminar flow. *J. Vis. Exp.* **2011**, doi:10.3791/2545.

23.	Fatoyinbo, H.O.; Hoettges, K.F.; Hughes, M.P. Rapid-on-chip determination of dielectric properties of biological cells using imaging techniques in a dielectrophoresis dot microsystem. *Electrophoresis* **2008**, *29*, 3–10.

24.	Pamme, N. Continuous flow separations in microfluidic devices. *Lab Chip* **2014**, *7*, 1644–1659.

25.	Jung, J.; Han, K.-H. Lateral-driven continuous magnetophoretic separation of blood cells. *Appl. Phys. Lett.* **2008**, *93*, doi:10.1063/1.3036898.

26.	Chen, P.; Huang, Y.Y.; Hoshino, K.; Zhang, X. Multiscale immunomagnetic enrichment of circulating tumor cells: From tubes to microchips. *Lab Chip* **2014**, *14*, 446–458.

27.	Jin, C.; McFaul, S.M.; Duffy, S.P.; Deng, X.; Tavassoli, P.; Black, P.C.; Ma, H. Technologies for label-free separation of circulating tumor cells: From historical foundations to recent developments. *Lab Chip* **2014**, *14*, 32–44.

28.	Kadri, N.A. *Development of Near Real-Time Asessment Systzem for Cancer Cells*; University of Surrey: Guildford, UK, 2010.

29.	Low, W.S.; Kadri, N.A.; Wan Abas, W.A.B.B. Computational fluid dynamics modelling of microfluidic channel for dielectrophoretic biomems application. *Sci. World J.* **2014**, *2014*, 11.

30.	Adams, J.; Olson, N.; Rawlins, J. *Microfluidic Final Report*; University of Lincoln: Lincoln, UK, 2015.

31.	Zborowski, M. Maxwell stress and magnetic force. In *Magnetic Cell Separation*; Zborowski, M., Chalmers, J.J., Eds.; Elsevier: Amsterdam, The Netherlands, 2008; pp. 62–78.

32. Friend, J.; Yeo, L. Fabrication of microfluidic devices using polydimethylsiloxane. *Biomicrofluidics* **2010**, *4*, doi:10.1063/1.3259624.

33. Association, M.M.P. *Standard Specifications for Permanent Magnet Materials*; International Electrotechnical Commision: Chicago, IL, USA, 2014.

34. Emerson, D.R.; Cieslicki, K.; Gu, X.; Barber, R.W. Biomimetic design of microfluidic manifolds based on a generalised Murray's law. *Lab Chip* **2006**, *6*, 447–454.